

Majorana Zero Modes in Cylindrical Semiconductor Quantum Wire

Chao Lei,^{1,2} Guru Khalsa,^{2,3} Jiangfeng Du,¹ and Allan H. MacDonald²

¹*Department of Modern Physics, University of Science and Technology of China, Hefei, Anhui 230026, China*

²*Department of Physics, The University of Texas at Austin, Austin, Texas 78712, USA*

³*Department of Materials Science and Engineering, Cornell University, Ithaca, New York 14853, USA*

We study Majorana zero modes properties in cylindrical cross-section semiconductor quantum wires based on the $\mathbf{k} \cdot \mathbf{p}$ theory and a discretized lattice model. Within this model the influence of disorder potentials in the wire and amplitude and phase fluctuations of the superconducting order-parameter are discussed. We find that for typical wire geometries, pairing potentials, and spin-orbit coupling strengths, coupling between quasi-one-dimensional sub-bands is weak, low-energy quasi-particles near the Fermi energy are nearly completely spin-polarized, and the number of electrons in the active sub-bands of topological states is small.

I. INTRODUCTION

One-dimensional (1D) p-wave superconductors are topologically nontrivial¹ and, in finite systems, support end-localized Majorana zero modes.² These states have attracted considerable interest lately³⁻⁹ because of their non-Abelian exchange properties,^{10,11} and related potential utility in quantum information processing systems³. Theory has suggested^{12,13} that it should be possible to engineer effective one-dimensional p-wave superconductors in proximity coupled semiconductor quantum wires by combining broken inversion symmetry, and the consequent Rashba spin-orbit interactions, with external magnetic fields. Considerable progress has been made in exploring this idea experimentally.¹⁴⁻⁴⁵ There has also been progress toward Majorana-based quantum state manipulation in other systems, including magnetic atom chains,⁴⁶⁻⁴⁸ interfaces between conventional superconductors and topological insulators,^{49,50} iron-based superconductors,⁵¹ and phase-controlled Josephson junctions.^{52,53}

The Majorana zero modes in semiconductor quantum wires⁵⁴⁻⁵⁷ are expected to appear only when external magnetic field strengths exceed a critical value, beyond which the proximity-induced superconductor gap vanishes. Early experiments in cylindrical cross section quantum wires exhibit many trends consistent with expectations¹⁴⁻¹⁹ based on Majorana zero mode properties, although they also consistently exhibit evidence of a soft gap, *i.e.* of quasiparticle states within the gap, at all magnetic field strengths. The in-gap states can be associated with spatially extended Andreev states,⁵⁸ disorder⁵⁹⁻⁶¹ or Kondo effects,⁶² and may influence electron transport experiments, and would poison any attempt to achieve topologically protected state manipulation.

In this paper, we study quasi-one-dimensional cylindrical quantum wires numerically, using experimentally realistic geometries diameters ~ 100 nm, as shown in Fig. 1), experimentally estimated pairing potential and spin-orbit coupling strengths, and a variety of types of experimentally realistic disorder. In experiment,

the longest quantum wires have approximate cylindrical cross-sections. Longer wires have weaker hybridization between Majorana zero modes at the ends of quantum wire, and more electrons in active subbands.

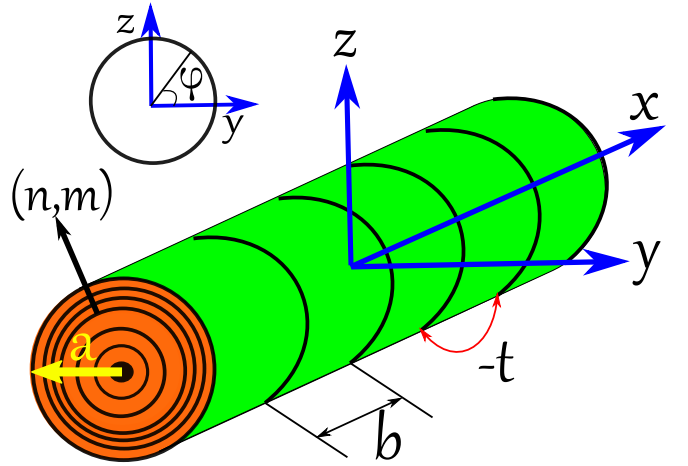


FIG. 1. (Color online). Cylindrical semiconductor quantum wire geometry. Here a labels the radius of the cylindrical quantum wire, b is the lattice constant used to discretize position along the wire in our numerical studies, and t the corresponding hopping strength. The circles in the cross-section schematically represent radial wavefunctions labeled by principal axial quantum number n and angular momentum m .

Our paper is organized as follows. In Section II we introduce a theoretical model for cylindrical quantum wires and discuss its topological-state phase diagram as a function of Fermi energy and magnetic field. In Section III we analyze the Andreev states, and the tunneling density of states as a function of magnetic field, disorder potential, and pairing-potential disorder in infinite quantum wires. In Section IV we address the case of finite length, using wire lengths on the scale of experimental samples and discuss finite-length Majorana energy splitting effects. In Section V we discuss the use of models in which only degrees of freedom in the semiconductor quantum wire are included explicitly, *vs.* models that account explicitly for the superconducting metal.

II. $k \cdot p$ THEORY

When Rashba spin-orbit interactions are neglected, the cylindrical-coordinate $\mathbf{k} \cdot \mathbf{p}$ Hamiltonian for an n -type semiconductor quantum wire oriented along the \hat{x} direction (shown in Fig. 1) separates into a free-particle contribution along the wire and a radial confinement contribution.^{63,64} The Hamiltonian is

$$\mathcal{H}_0 = \frac{\hbar^2}{2m^*} \left(k_x^2 - \frac{\partial^2}{\partial r^2} - \frac{1}{r} \frac{\partial}{\partial r} - \frac{1}{r^2} \frac{\partial^2}{\partial \varphi^2} \right) + V(\mathbf{r}, x) \quad (1)$$

where \hbar is Planck's constant, m^* is the conduction band effective mass, $V(\mathbf{r}, x)$ is the confining potential, $\mathbf{r} = (y, z) = (r \cos(\varphi), r \sin(\varphi))$ is the position projected to the wire cross-section, x is position along the wire, and k_x is wave vector along the wire. In the absence of disorder, we take $V(\mathbf{r}, x)$ to be 0 inside the wire ($|\mathbf{r}| < a$ where a the radius of the wire) and $+\infty$ outside the wire.

Cylindrical symmetry implies that eigenstates can be labeled by angular momentum m along the wire axis. The confined radial wave functions are then Bessel functions with zeros at the wire edge. The one-dimensional transverse wave-functions are

$$f_{n,m}(r, \varphi) = A_{n,m} J_{|m|} \left(u_{n,m} \frac{r}{a} \right) e^{im\varphi}, \quad m = 0, \pm 1, \pm 2, \dots \quad (2)$$

where $J_{|m|}(u_{n,m} \frac{r}{a})$ is an m^{th} -order Bessel function, $u_{n,m}$ is the n^{th} zero of the m^{th} -order Bessel function, and $A_{n,m} = 1/[a\sqrt{\pi}J_{|m|+1}(u_{n,m})]$ is a normalization constant. The one-dimensional sub-bands are rigidly offset by an energy which is determined by the principal axial quantum number n and the azimuthal quantum number m that quantifies the angular momentum, the dispersion is

$$E_{n,m}(k_x) = \frac{\hbar^2}{2m^*} k_x^2 + \frac{\hbar^2}{2m^*} \frac{u_{n,m}^2}{a^2}. \quad (3)$$

Note that since $u_{n,m} = u_{n,-m}$ so $|m| \neq 0$ sub-bands are always doubly degenerate.

The one-dimensional band structure with quantum numbers labeled by (n,m) is illustrated in Fig. 2. These results were obtained by using parameters that are appropriate for the $a = 50$ nm InSb quantum wire ($m^* = 0.015m_e$) studied in the first Majorana experiment¹⁴ with Rashba coupling parameter $\alpha = 0.02$ eV · nm. We note that subsequent experiments studied quantum wires with similar properties. Rashba spin-orbit interactions lift the $m = \pm 1$ degeneracy and for finite k_x and lift the spin-degeneracy within each sub-band.

The mean-field Hamiltonian of a spin-orbit coupled quantum wire with proximity-induced s -wave superconductivity and an external magnetic field includes one-dimensional sub-band, Rashba, Zeeman, and pairing contributions:

$$\mathcal{H} = \mathcal{H}_0 + \mathcal{H}_R + \mathcal{H}_Z + \mathcal{H}_{SC} \quad (4)$$

It is convenient to express this Hamiltonian in the representation of parabolic band quantum wire eigenstates.

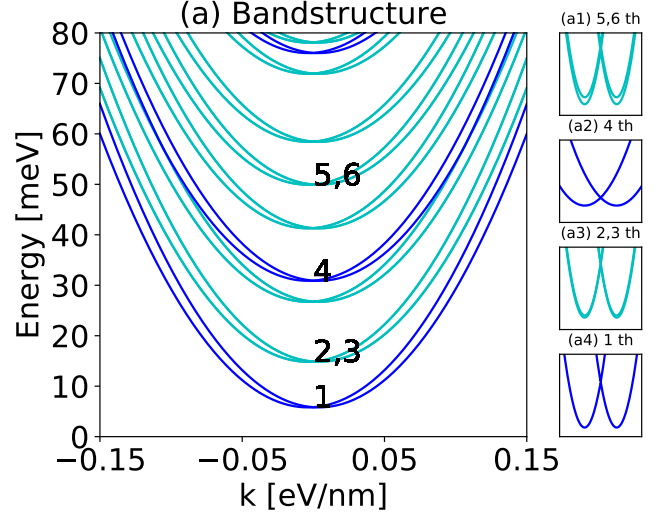


FIG. 2. (Color online). One-dimensional band-structure of a cylindrical semiconductor quantum wire with radius $a = 50$ nm, InSb conduction band mass $m^* = 0.015m_e$, and Rashba coupling parameter $\alpha = 0.02$ eV · nm. The panels on the right highlight the behaviors near band minima, which are important for topological superconductivity. Angular momentum m is not a good quantum number for finite Rashba coupling strength. Because the Rashba interaction couples only states that differ by ± 1 in angular momentum. The mixing between $m = 1$ and $m = -1$ sub-bands is second-order in the ratio of the Rashba coupling strength ($\sim \alpha/a$) to the sub-band separations, which is small.

Assuming that the quantum wire is placed on a substrate with a \hat{z} direction surface normal, the quantum wire Rashba Hamiltonian is

$$\mathcal{H}_R = \alpha \left[-i(\cos \varphi \frac{\partial}{\partial r} - \frac{\sin \varphi}{r} \frac{\partial}{\partial \varphi}) \sigma_x - k_x \sigma_y \right], \quad (5)$$

where α is the Rashba coupling parameter and σ_α is a Pauli matrix acting on spin. The matrix elements of the Rashba Hamiltonian in the representation of unperturbed band states are

$$\langle n, m | \mathcal{H}_R | n', m' \rangle = -\alpha k_x \sigma_y \delta_{n,n'} \delta_{m,m'} - i\alpha R_{nm;n'm'} \sigma_x, \quad (6)$$

where

$$R_{nmn'm'} = \langle f_{nm} | \left(\cos \theta \frac{\partial}{\partial r} - \frac{\sin \theta}{r} \frac{\partial}{\partial \theta} \right) | f_{n'm'} \rangle \quad (7)$$

is non-zero for $m = m' \pm 1$.

The Zeeman Hamiltonian can be written as: $\mathcal{H}_Z = \mathbf{B} \cdot \boldsymbol{\sigma}$ where \mathbf{B} is the magnetic field expressed in energy units. In most experiments the magnetic field is along the \hat{x} direction. The proximity-induced s -wave pairing contribution to the Hamiltonian is

$$\mathcal{H}_{SC} = \sum_{n,m} \left[\Delta_{SC}^* c_{n,m,\downarrow}^\dagger c_{n,m,\uparrow}^\dagger + \Delta_{SC} c_{n,m,\uparrow} c_{n,m,\downarrow} \right], \quad (8)$$

where $\Delta_{SC} = |\Delta_{SC}|e^{i\phi}$ is the proximity induced gap. The value of Δ_{SC} depends on a complex hybridization processes between orbitals in the quantum wire and orbitals in the surrounding superconductor but can be fit to experimental observations. The relatively large values of Δ_{SC} (0.25 meV in Ref. 14 for example) suggest that the interface between the quantum wire and the surrounding superconductor is quite transparent. We will return to this point in the discussion section.

Topologically distinct phases are separated in coupling-constant parameter space by gapless boundary states. In the case of topological superconductivity in quantum wires, the coupling constants that are readily varied in experiments are the position of the Fermi level relative to the conduction band minimum, which can be altered by manipulating gate voltages, and the strength of the magnetic field responsible for Zeeman coupling to the spin degree of freedom. In the absence of an external magnetic field all states are topologically trivial. As the magnetic field strength is increased, the energy gap produced by the proximity effect pairing potential sometimes closes at discrete points. The phase diagram in Fig.3 was constructed by tracking these band closings and identifying each with a phase transition from a topologically trivial to a nontrivial state. While increasing the magnetic field with the Fermi level positioned near a sub-band, the superconductor gap closes when the system is driven from trivial superconductivity to non-trivial topological superconductivity. The phase diagram can be found by tuning the Fermi level and magnetic field (shown as Fig. 3). When the Zeeman Energy exceed the pairing potential while the Fermi level is tuned to lie at the bottom of a sub-bands a Majorana(-like) zero-mode phase appears. For sub-bands $n = 1, 2$ and $m = 0, \pm 1$ (see Fig.3), these six sub-bands have the Fermi energy of $E_{F1} \approx 5.87$ meV, $E_{F2} \approx E_{F3} \approx 14.9$ meV, $E_{F4} \approx 30.96$ meV and $E_{F5} \approx E_{F6} \approx 50$ meV. In the phase diagram we use Roman numerals to label the number of Majorana-like end-localized states. (*I* – one localized state, *II* – two localized states, etc.) The bottom panel of Fig. 3 shows the phase diagram for small Zeeman energy where we note that more detail can be seen. Due to the lack of degeneracy of the sub-bands in Fig. 3(b,d) we expect robust Majorana modes, but in Fig. 3(c,e) where sub-bands are nearly degenerate, we expect Majorana-like modes that are weakly coupled.

III. ANDREEV STATES

In contrast to the Majorana modes, zero-bias conductance peaks (ZBCP) in transport experiments may also come from Andreev states which was recently studied experimentally.²¹ Here we distinguish the evolution of Andreev states from Majorana zero modes by varying the magnetic field. From the discussion of Section II, we see that there are degenerate sub-bands which are

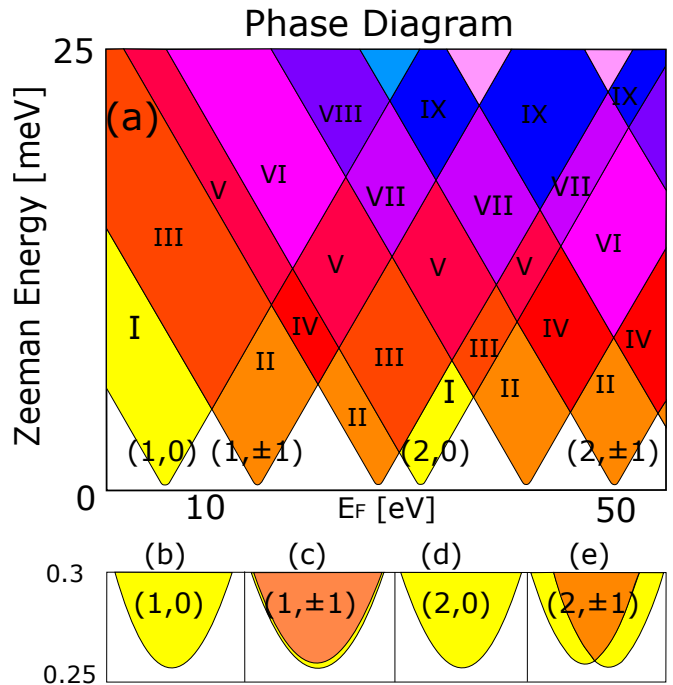


FIG. 3. (Color online). Phase diagram of the cylindrical semiconductor quantum wire as a function of Fermi level and magnetic field. (a) At each sub-band there appears Majorana(-like) zero-modes when the magnetic field exceeds the pairing potential and the Fermi level is tuned to the bottom of the sub-bands, of which $n = 1, 2$ and $m = 0, \pm 1$ sub-bands have the Fermi energy at $E_{F1} \approx 5.87$ meV, $E_{F2} \approx E_{F3} \approx 14.9$ meV, $E_{F4} \approx 30.96$ meV and $E_{F5} \approx E_{F6} \approx 50$ meV. In the figure we use Roman numerals and color coordination to label the number of Majorana-like end-localized states. (b-e) Phase diagram focused near the band minima for different (n,m) .

weakly coupled by Rashba interactions for non-zero angular momentum, while the zero-angular momentum sub-bands are not degenerated. To find the energy spectrum for finite wires we use a quantization and discretization scheme that takes $kx \rightarrow -i\partial/\partial x$ and $\partial^2 c(x)/\partial x^2 \approx (c_{i+1} + c_{i-1} - 2c_i)/b^2$ and $\partial c(x)/\partial x \approx (c_{i+1} - c_{i-1})/2b$, where b is the effective lattice constant shown in Fig. 1. In the following calculations we will set b to be 5 nm.

With periodic boundary condition, that is $c_{N+1} = c_1$, there are no Majorana zero modes, and only Andreev states (shown as Fig. 4). Fig. 4 (a)-(c) is the density of states (DOS) of the sub-bands with quantum number of $(n,m)=(1,0), (1,\pm 1)$ and $(2,0)$. We reiterate that the sub-bands with quantum number $(1,\pm 1)$ are weakly coupled through coupling to other sub-bands, as previously discussed. The DOS when Fermi level is tuned at the bottom of the lowest sub-band (that with quantum number of $(n,m)=(1,0)$) is shown in Fig. 4 (a) with the Zeeman energy varying from 0 to $4\Delta_{SC}$ and the edges of the superconducting gap labeled with red arrows. When the magnetic field increases, a pair of Andreev states cross when the Zeeman energy equals the pairing potential. When the periodic boundary condition is removed, that

is for finite length quantum wires, the pair of Andreev states evolve into Majorana zero-modes, which remain at zero energy once the Zeeman energy exceeds the pairing potential as in Fig. 4 (d).

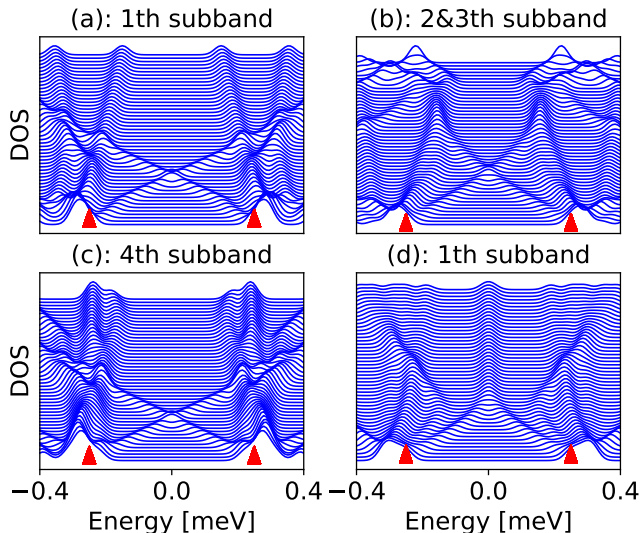


FIG. 4. (Color online). Envolvement of Andreev states and Majorana zero modes versus magnetic field. (a)-(c) show the DOS of the infinite wire when the Fermi level is tuned at the bottom of sub-bands with different quantum numbers. The magnetic field changes from 0 to $B = 4\Delta_{SC}$ where $\Delta_{SC} = 0.25\text{meV}$. The lines are separated by Zeeman energy of 0.02meV . (d) DOS for finite quantum wire with Fermi level tuned to the bottom of the $(n,m) = (1,0)$ sub-band. The pair of Andreev states evolve into the Majorana zero modes when the Zeeman energy exceed the pairing potential in this case.

It has been argued that the zero-bias peak observed in experiment can also be caused by disorder.⁵⁹⁻⁶¹ Here we construct a binary disorder model for the chemical potential and pairing potential and use a Gaussian distribution model of the pairing phase disorder. When the Fermi level lies at the lowest sub-bands, that with $(n,m) = (1,0)$, the DOS of the infinite wire with different kind of disorder are shown in Fig. 5 (a)-(c). To model a charge disorder in the semiconductor we define a spatially varying chemical potential $\mu_i = \mu \pm \delta\mu$ where $\delta\mu = |\Delta_{SC}|$ sampled randomly for each site i . We find that the DOS is insensitive to this type of disorder (Fig. 5 (a)). However, this is not the case for disorder in the phase and amplitude of the superconducting order-parameter (Fig. 5(b) and (c)). The disorder is modeled by setting $|\Delta_{SC,i}|$ to be 0 and $|\Delta_{SC}|$ randomly for disorder in the pairing potential. Disorder in the phase is model as:

$$\Delta_{SC,i} = |\Delta_{SC}|e^{i(\phi_0 + \delta\phi_i)}, \quad (9)$$

where ϕ_0 is the average phase of the pairing, and the statistics of $\delta\phi_i$ are sampled from a Gaussian function:

$$f(\delta\phi_i) = (1/\sqrt{2\pi}\sigma)e^{-\delta\phi_i^2/2\sigma^2}. \quad (10)$$

We set the variance of the phase to be bounded by $\sigma = \pi/2$. Disorder in the amplitude and phase lead to substantial changes of the superconductivity gap. From these simulations we see that if we only consider the proximity effect, the experimental finding that the density of in-gap states is much smaller the DOS at the edge of superconducting gap cannot be explained. This suggests that electrons from the superconducting metal may contribute significantly to the experimental DOS.

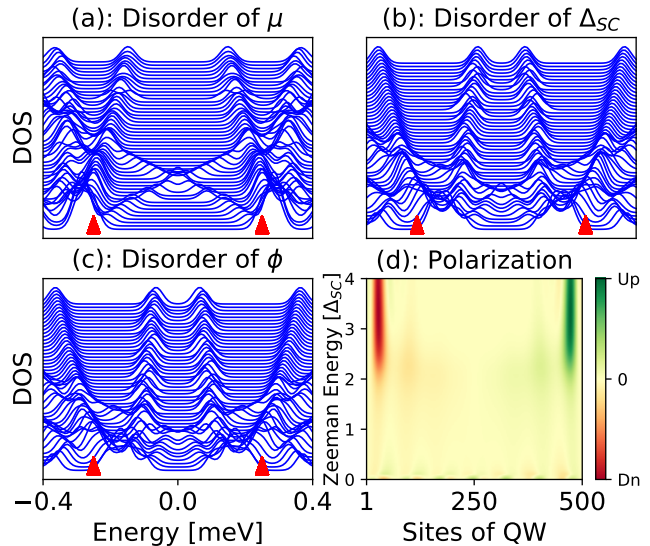


FIG. 5. (Color online). The effect of disorder and magnetic field on Andreev states. (a)-(c) DOS of the infinite wire at the lowest band with different types of disorder: (a) disorder in the chemical potential with $\mu_i = \mu \pm \delta\mu$ where $\delta\mu = 0, \pm\Delta_{SC}$ by random; (b) pairing amplitude disorder with $\Delta_{SC}^i = 0, \Delta_{SC}$; (c) pairing phase disorder modeled as a normal distribution, with the mean phase as 0 and the variance of the phase as $\pi/2$; (d) The polarization $n_\uparrow - n_\downarrow$ of Andreev states along the quantum wire (here $L = 1\ \mu\text{m}$ with periodic boundary conditions).

IV. MAJORANA ZERO MODES PROPERTIES

In the previous section, it was shown that disorder in the pairing potential decreases the size of the superconductor gap. We now extend this discussion – using the same model and model parameters¹⁴ – now used to describe a finite quantum wire with length of $1\ \mu\text{m}$. Fig. 6 (a)-(c) shows the DOS versus the Zeeman energy for disorder in the chemical potential, and superconducting order-parameter amplitude, and phase, respectively. The superconductivity gap is robust to disorder in the chemical potential but again decreases with disorder in the superconducting order-parameter amplitude and phase. We find that the critical magnetic field decreases by almost a factor of 2 in the finite wire when disorder in the order-parameter is included.

This sensitivity to magnetic field found in the finite system is not only a symptom of disorder. The Majorana modes in the finite system are more sensitive to magnetic field than the Andreev states seen in the infinite system even in the absence of disorder. The polarization of the two states closest to zero energy, calculated as $n_{\uparrow} - n_{\downarrow}$ in Fig. 6(d) show that the Zeeman energy needed to polarize the Majorana modes is the size of the pairing potential. This can be compared to Fig. 5(d) showing the same quantity in the infinite wire where the Zeeman energy required to polarize these states is a factor of ≈ 2 times the pairing potential. With these results we find that the Andreev bound states in the infinite wire require a larger Zeeman energy to polarize than the Majorana zero-modes even in the absence of disorder.

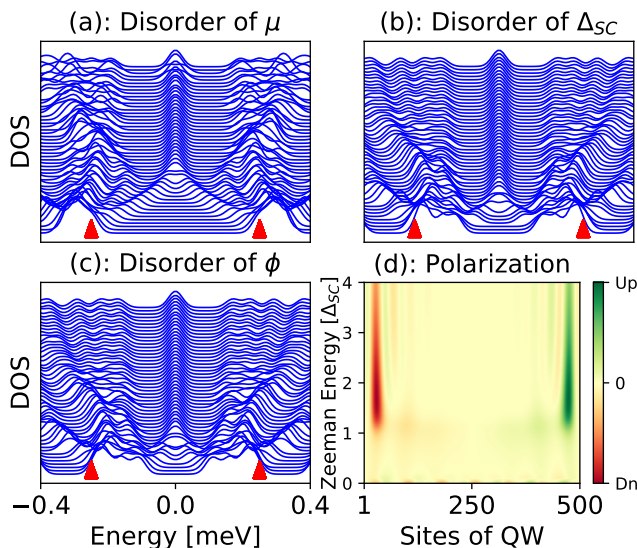


FIG. 6. (Color online). DOS at the lowest sub-band with quantum number $(n,m) = (1,0)$ in the finite quantum wire. The magnetic field changes from 0 at the bottom of the plots in increments of 0.02 meV up to $B = 4\Delta_{SC}$ at the top of the plots. Again, the pairing potential is $\Delta_{SC} = 0.25 \text{ meV}$. (a) Disorder in the chemical potential; (b) Disorder of pairing amplitude; (c) Disorder of pairing phase; (d) Polarization of Majorana zero modes along the quantum wire (with $L = 1 \mu m$).

In tunneling experiments on proximitized quantum wire systems, the local density of states at the end of the quantum wire is probed. The DOS at the edge of the superconducting gap is found to be larger than the zero-biased peak associated with Majorana modes. We can probe this feature in our model by calculating the projected DOS for different length-scales measured from the end of the wire. Fig. 7 (a) and (b) shows the projected DOS parameterized by the Zeeman energy for states projected within 50 nm , and 250 nm from the end of the wire. We note again that the length of the wire in this simulation is $1 \mu m$. In this way we can compare states at the end of the wire with the bulk system. While we find the

DOS near the edge of the gap is small when we focus on the end of the wire (Fig. 7 (a)), this become comparable with the zero-bias peak when we include bulk states (Fig. 7 (b)). The size of the DOS at the superconducting gap energy relative to the zero-bias peak found in experiment, cannot be accounted for in this model.

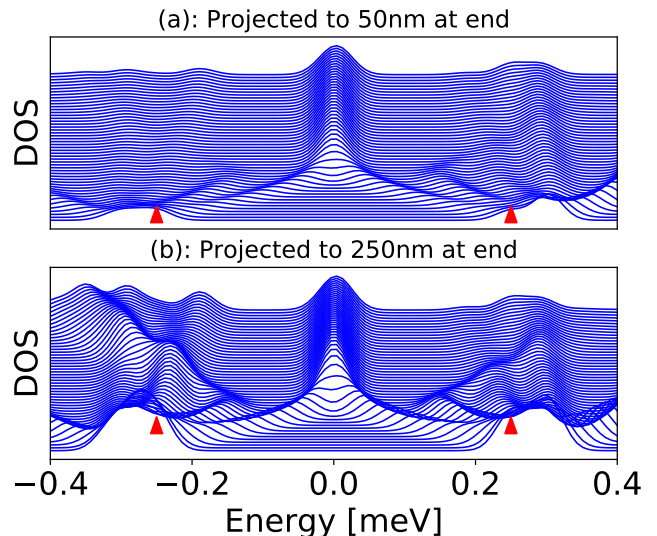


FIG. 7. (Color online). Projected DOS at the end of the quantum wire. (a) is the results of DOS projected at the end within 50 nm and (b) is the results of DOS projected at the end within 250 nm .

V. DISCUSSION

In this paper we have studied the properties of cylindrical semiconducting quantum wires proximity coupled to a superconductor. Topological states occur in the presence of an external magnetic field for Fermi levels just above the population thresholds of all angular momentum $m = 0$ quasi-one-dimensional sub-bands. For long but finite cylindrical wires, Majorana zero modes are localized near wire-ends at $m = 0$ sub-band population thresholds. In contrast, pairs of localized Majorana-like states appear at each end near the populations thresholds of degenerated sub-bands which can give rise to zero-bias anomalies in transport – although they are not strictly speaking associated with topological states.

By modeling the influence of disorder within quantum wires we conclude that if only the proximity effect in semiconductor quantum wire is considered, the only effect of pairing(or phase) potential is to give a smaller observable superconducting gap, disorder within the quantum wires is thus not on its own able to account for the discrepancies between naive quantum-wire theory and experimental findings. We suggest instead that the current-path followed in the transport experiments used to probe semiconductor quantum wires is strongly influenced by sub-gap states in the superconducting metal

which surrounds the quantum wire and is used to induce superconductivity within it.

The DOS measured in experiment strongly depends on not only the Majorana zero modes spectrum, but also the superconducting element which donates its superconductivity to the semiconductor quantum wire. We clarify this point by estimating the semiconductor and metal (superconductor) electron density for direct comparison (See Appendix A for details).

We find that the number of electrons in the metal/superconductor N_{sc} greatly outnumbers the number of electrons in the semiconductor N_{qw} ($N_{sc} \gg N_{qw}$), with their ratio ranging from $\sim 10^3$ to $\sim 10^5$ depending on the specific materials. Summarized in Table I, are the estimates of the electron count. The number of electrons in the superconducting metal is many orders of magnitude larger than the number of electrons in the semiconductor quantum wire.

TABLE I. Extracted experimental parameters. Ratio of the superconducting pairing potential Δ to the spin-orbit energy E_{so} , the number of electrons in the quantum wire N_{qw} , and the ratio of the number of electrons in the superconductor N_{sc} to the number of electrons in the quantum wire.

Materials	Δ/E_{so}	N_{qw}	N_{sc}/N_{qw}
InSb/Nb ¹⁴	0.8	5.0	2.0×10^5
InSb/Nb ¹⁹	0.6	1.4	2.3×10^4
InAs/Al ¹⁶	0.8	0.4	1.3×10^4
Nb/InSb/Nb ¹⁵	0.3	3.0	1.4×10^5
InSb/NbTiN ¹⁷	1.4	0.6	2.3×10^5
InAs/NbN ¹⁸	16.5	1.9	4.8×10^4
InAs/Al ^{20,21,26}	2.1	0.6-2.5	9.3×10^2

This shows that electrons in the superconducting metals will play an important role in understanding measurements of Majorana zero-modes in proximatized quantum wires. A complete model that include both electrons in semiconductor quantum wires and superconducting metal⁹ is thus necessary.

The present proximitized semiconductor quantum wire based Majorana systems may be in fact treated as a superconducting metal perturbed by magnetic field and spin-orbit interaction proximitized by semiconductor quantum wires, the main contribution to the tunneling DOS come from the electrons in superconducting metal instead of the semiconductor quantum wire. Ultrathin film metals with strong spin-orbit coupling⁶⁵ are thus a prospective platform to realize topological superconductors if the g-factor is large enough and effective tools are found to tune the Fermi level.

VI. ACKNOWLEDGEMENTS

This work was financially supported by Welch Foundation under grant TBF1473 and by Army Research Office under Grant Number W911NF-16-1-0472.

Appendix A: Estimation of experimental parameters

To estimate the electrons involved in Majorana zero modes in semiconductor quantum wire, we consider the active sub-band and model it with the follow quasi-one-dimensional Hamiltonian:

$$H_k = \frac{\hbar^2}{2m^*}k^2 + \alpha k\sigma_y \quad (\text{A1})$$

where \hbar is the reduced Plank constant, m^* is the effective mass of electrons in semiconductor, α is the Rashba coupling. The band energy can be solved to be:

$$E_k = \frac{\hbar^2}{2m^*}k^2 \pm \alpha k. \quad (\text{A2})$$

To estimate the number of electron in the semiconductor quantum wires N_{qw} , we take advantage of the quasi-1D nature of the wires and find $N_{qw} = \frac{k_{so} \cdot L}{\pi}$ (see Table I). Here $k_{so} = \frac{2\alpha m^*}{\hbar^2}$ is the spin-orbit wave vector and L is the length of quantum wire. This assumes that the chemical potential has been tuned to E_{so} by the gate voltage. The spin-orbit wave vector and spin-orbit energy $E_{so} = \frac{\alpha^2 m^*}{2\hbar^2} = \frac{\alpha}{4}k_{so}$ are estimated from the extracted experimental effective electron mass m^* and Rashba coupling α . The estimation of the experimental parameters in semiconductor quantum wire are shown in Table II.

Via proximity effect, the Cooper pairs tunnel into the quantum wire, the DOS in Aluminum is

$$D(E_F) = \frac{m^*}{\pi^2 \hbar^3} \sqrt{2m^* E_F} = \frac{2m^*}{\hbar^2 k_F^2} \frac{\hbar^2 k_F^2}{2\pi^2} \sqrt{\frac{2m^*}{\hbar^2} E_F} \quad (\text{A3})$$

since $E_F = \frac{\hbar^2 k_F^2}{2m^*}$, then

$$D(E_F) = \frac{1}{E_F} \frac{k_F^2}{2\pi^2} \sqrt{\frac{1}{E_F} k_F^2 E_F} = \frac{1}{E_F} \frac{k_F^3}{2\pi^2} \quad (\text{A4})$$

while the density of free electron in 3D system is $n = \frac{2 \cdot 4\pi k_F^3}{(2\pi)^3} \rightarrow k_F^3 = 3\pi^2 n$, then the DOS is

$$D(E_F) = \frac{3n}{2E_F} \quad (\text{A5})$$

To calculate the number density of free electrons (n):

$$n = z \frac{N_A}{V_A} \quad (\text{A6})$$

where z is the valency, N_A is the Avogadros constant, V_A is the molar volume. To calculate the molar volume:

$$V_A = \frac{M_r \times 10^{-3}}{\rho} \quad (\text{A7})$$

where M_r is the relative atomic mass (the 10^{-3} is to convert M_r from grams to kg), ρ is the density. We then get

$$n = \frac{z\rho N_A}{M_r \times 10^{-3}} \quad (\text{A8})$$

TABLE II. Summary of parameters of semiconductor quantum wires.

Materials	Geometry	L[nm]	α [eVnm]	m^* [m_e]	k_{so} [nm^{-1}]	λ_F [nm]	r_{ee} [nm]	E_{so} [meV]	N_{qw}
InSb/Nb ¹⁴	Cir	~ 2000	0.02	0.015	0.0079	127	399	0.315	5
InSb/Nb ¹⁹	Ret	~ 600	0.019	0.015	0.0075	134	420	0.284	1.4
InAs/Al ¹⁶	Cir	~ 150	0.0113	0.03	0.0089	112	353	0.201	0.4
Nb/InSb/Nb ¹⁵	Cir	$\sim 740(680)$	0.032	0.015	0.0126	79	250	0.806	3(2.7)
InSb/NbTiN ¹⁷	Cir	~ 250	0.02	0.015	0.0079	127	399	0.315	0.6
InAs/NbN ¹⁸	Cir	~ 1000	0.01	0.023	0.006	166	520	0.121	1.9
InAs/Al ^{20,21,26}	Hex	330 – 1500	0.008	0.025	0.0052	190	598	0.084	0.6-2.5

For Aluminum $z = 3$ and $M_r = 27$, while for Niobium, $z = 5$ and $M_r = 93$, and the Avogadro constant is 6.02×10^{23} , then $n = 1.8 \times 10^{29} m^{-3}$ for Aluminum and $n = 2.8 \times 10^{29} m^{-3}$ for Niobium.

The number of electron in the superconducting metal is estimated by:

$$N_{so} = D(E_F) \cdot E_{so} \cdot V_{sc} = \frac{3n}{2} \frac{E_{so}}{E_F} \cdot V_{sc}, \quad (A9)$$

where V_{sc} is the volume of the superconducting shell, this expression for N_{sc} assumes that the DOS is constant on the scale of E_{so} and that only electrons near E_{so} contribute, the corresponding parameters estimated

from experiments are shown in Tabel III.

TABLE III. Summary of parameters of superconducting metals.

Materials	V_{SC} [$10^6 nm^3$]	Δ [meV]	N_{sc} [10^4]
InSb/Nb ¹⁴	40	0.25	99.46
InSb/Nb ¹⁹	1.44	0.18	3.23
InAs/Al ¹⁶	1.18	0.15	0.55
Nb/InSb/Nb ¹⁵	6.65(6.11)	0.25	42.33(38.89)
InSb/NbTiN ¹⁷	5.89	0.45	14.65
InAs/NbN ¹⁸	9.64	2	9.19
InAs/Al ^{20,21,26}	0.264-1.2	0.18	0.05-0.23

- ¹ A. Y. Kitaev, *Physics-Uspekhi* **44**, 131 (2001).
- ² E. Majorana, *Il Nuovo Cimento* **14**, 171 (1937).
- ³ C. Nayak, S. H. Simon, A. Stern, M. Freedman, and S. Das Sarma, *Rev. Mod. Phys.* **80**, 1083 (2008).
- ⁴ J. Alicea, *Reports on Progress in Physics* **75**, 076501 (2012).
- ⁵ C. Beenakker, *Annu. Rev. Condens. Matter Phys.* **4**, 113 (2013).
- ⁶ S. R. Elliott and M. Franz, *Rev. Mod. Phys.* **87**, 137 (2015).
- ⁷ R. M. Lutchyn, E. P. A. M. Bakkers, L. P. Kouwenhoven, P. Krogstrup, C. M. Marcus, and Y. Oreg, *Nature Reviews Materials* **3**, 5268 (2018).
- ⁸ M. Leijnse and K. Flensberg, *Semiconductor Science and Technology* **27**, 124003 (2012).
- ⁹ T. D. Stanescu and S. Tewari, *Journal of Physics: Condensed Matter* **25**, 233201 (2013).
- ¹⁰ N. Read and D. Green, *Phys. Rev. B* **61**, 10267 (2000).
- ¹¹ D. A. Ivanov, *Phys. Rev. Lett.* **86**, 268 (2001).
- ¹² R. M. Lutchyn, J. D. Sau, and S. Das Sarma, *Phys. Rev. Lett.* **105**, 077001 (2010).
- ¹³ Y. Oreg, G. Refael, and F. von Oppen, *Phys. Rev. Lett.* **105**, 177002 (2010).
- ¹⁴ V. Mourik, K. Zuo, S. Frolov, S. Plissard, E. Bakkers, and L. Kouwenhoven, *Science* **336**, 1003 (2012).
- ¹⁵ M. Deng, C. Yu, G. Huang, M. Larsson, P. Caroff, and H. Xu, *Nano letters* **12**, 6414 (2012).
- ¹⁶ A. Das, Y. Ronen, Y. Most, Y. Oreg, M. Heiblum, and H. Shtrikman, *Nature Physics* **8**, 887 (2012).
- ¹⁷ H. O. H. Churchill, V. Fatemi, K. Grove-Rasmussen, M. T. Deng, P. Caroff, H. Q. Xu, and C. M. Marcus, *Phys. Rev. B* **87**, 241401 (2013).
- ¹⁸ A. D. K. Finck, D. J. Van Harlingen, P. K. Mohseni, K. Jung, and X. Li, *Phys. Rev. Lett.* **110**, 126406 (2013).
- ¹⁹ L. P. Rokhinson, X. Liu, and J. K. Furdyna, *Nature Physics* **8**, 795 (2012).
- ²⁰ S. M. Albrecht, A. Higginbotham, M. Madsen, F. Kuemmeth, T. S. Jespersen, J. Nygård, P. Krogstrup, and C. Marcus, *Nature* **531**, 206 (2016).
- ²¹ M. T. Deng, S. Vaitiekenas, E. B. Hansen, J. Danon, M. Leijnse, K. Flensberg, J. Nygård, P. Krogstrup, and C. M. Marcus, *Science* **354**, 1557 (2016).
- ²² Ö. Gül, H. Zhang, J. D. Bommer, M. W. de Moor, D. Car, S. R. Plissard, E. P. Bakkers, A. Geresdi, K. Watanabe, T. Taniguchi, *et al.*, *Nature nanotechnology* **13**, 192 (2018).
- ²³ J. Chen, P. Yu, J. Stenger, M. Hoeschele, D. Car, S. R. Plissard, E. P. A. M. Bakkers, T. D. Stanescu, and S. M. Frolov, *Science Advances* **3** (2017), 10.1126/sciadv.1701476, <http://advances.sciencemag.org/content/3/9/e1701476.full.pdf>.
- ²⁴ H. J. Suominen, M. Kjaergaard, A. R. Hamilton, J. Shabani, C. J. Palmström, C. M. Marcus, and F. Nichele, *Phys. Rev. Lett.* **119**, 176805 (2017).
- ²⁵ F. Nichele, A. C. C. Drachmann, A. M. Whiticar, E. C. T. O'Farrell, H. J. Suominen, A. Fornieri, T. Wang, G. C. Gardner, C. Thomas, A. T. Hatke, P. Krogstrup, M. J. Manfra, K. Flensberg, and C. M. Marcus, *Phys. Rev. Lett.* **119**, 136803 (2017).
- ²⁶ H. Zhang, C.-X. Liu, S. Gazibegovic, D. Xu, J. A. Logan, G. Wang, N. van Loo, J. D. S. Bommer, M. W. A. de Moor, D. Car, and *et al.*, *Nature* **556**, 7479 (2018).
- ²⁷ J. E. Sestoft, T. Kanne, A. N. Gejl, M. von Soosten, J. S.

- Yodh, D. Sherman, B. Tarasinski, M. Wimmer, E. Johnson, M. Deng, J. Nygård, T. S. Jespersen, C. M. Marcus, and P. Krogstrup, *Phys. Rev. Materials* **2**, 044202 (2018).
- ²⁸ M.-T. Deng, S. Vaitiekėnas, E. Prada, P. San-Jose, J. Nygård, P. Krogstrup, R. Aguado, and C. M. Marcus, *Phys. Rev. B* **98**, 085125 (2018).
- ²⁹ S. Vaitiekėnas, G. W. Winkler, B. van Heck, T. Karzig, M.-T. Deng, K. Flensberg, L. I. Glazman, C. Nayak, P. Krogstrup, R. M. Lutchyn, and et al., *Science* **367**, eaav3392 (2020).
- ³⁰ S.-B. Zhang, A. Calzona, and B. Trauzettel, “All-electrically tunable networks of majorana bound states,” (2020), [arXiv:2003.04053 \[cond-mat.supr-con\]](https://arxiv.org/abs/2003.04053).
- ³¹ X. P. Zhang, V. N. Golovach, F. Giazotto, and F. S. Bergeret, *Phys. Rev. B* **101**, 180502 (2020).
- ³² X.-Q. Li and L. Xu, *Phys. Rev. B* **101**, 205401 (2020).
- ³³ J. Ekström, P. Recher, and T. L. Schmidt, *Phys. Rev. B* **101**, 195420 (2020).
- ³⁴ J. S. Lee, B. Shojaei, M. Pendharkar, A. P. McFadden, Y. Kim, H. J. Suominen, M. Kjaergaard, F. Nichele, H. Zhang, C. M. Marcus, and et al., *Nano Letters* **19**, 30833090 (2019).
- ³⁵ L. S. Ricco, M. de Souza, M. S. Figueira, I. A. Shelykh, and A. C. Seridonio, *Phys. Rev. B* **99**, 155159 (2019).
- ³⁶ G. W. Winkler, A. E. Antipov, B. van Heck, A. A. Soluyanov, L. I. Glazman, M. Wimmer, and R. M. Lutchyn, *Phys. Rev. B* **99**, 245408 (2019).
- ³⁷ A. E. Antipov, A. Bargerbos, G. W. Winkler, B. Bauer, E. Rossi, and R. M. Lutchyn, *Phys. Rev. X* **8**, 031041 (2018).
- ³⁸ C. Chan, L. Zhang, T. F. J. Poon, Y.-P. He, Y.-Q. Wang, and X.-J. Liu, *Phys. Rev. Lett.* **119**, 047001 (2017).
- ³⁹ M. Kjaergaard, F. Nichele, H. J. Suominen, M. Nowak, M. Wimmer, A. Akhmerov, J. Folk, K. Flensberg, J. Shabani, w. C. Palmstrøm, et al., *Nature communications* **7**, 12841 (2016).
- ⁴⁰ F. Nichele, A. C. C. Drachmann, A. M. Whitarcar, E. C. T. O’Farrell, H. J. Suominen, A. Fornieri, T. Wang, G. C. Gardner, C. Thomas, A. T. Hatke, P. Krogstrup, M. J. Manfra, K. Flensberg, and C. M. Marcus, *Phys. Rev. Lett.* **119**, 136803 (2017).
- ⁴¹ C. Böttcher, F. Nichele, M. Kjaergaard, H. Suominen, J. Shabani, C. Palmstrøm, and C. Marcus, *Nature Physics* **14**, 1138 (2018).
- ⁴² F. Pientka, A. Keselman, E. Berg, A. Yacoby, A. Stern, and B. I. Halperin, *Phys. Rev. X* **7**, 021032 (2017).
- ⁴³ J. Shabani, M. Kjaergaard, H. J. Suominen, Y. Kim, F. Nichele, K. Pakrouski, T. Stankevic, R. M. Lutchyn, P. Krogstrup, R. Feidenhans’l, S. Kraemer, C. Nayak, M. Troyer, C. M. Marcus, and C. J. Palmstrøm, *Phys. Rev. B* **93**, 155402 (2016).
- ⁴⁴ M. Hell, M. Leijnse, and K. Flensberg, *Phys. Rev. Lett.* **118**, 107701 (2017).
- ⁴⁵ H. J. Suominen, M. Kjaergaard, A. R. Hamilton, J. Shabani, C. J. Palmstrøm, C. M. Marcus, and F. Nichele, *Phys. Rev. Lett.* **119**, 176805 (2017).
- ⁴⁶ S. Nadj-Perge, I. K. Drozdov, J. Li, H. Chen, S. Jeon, J. Seo, A. H. MacDonald, B. A. Bernevig, and A. Yazdani, *Science* **346**, 602 (2014).
- ⁴⁷ R. Pawlak, M. Kisiel, J. Klinovaja, T. Meier, S. Kawai, T. Glatzel, D. Loss, and E. Meyer, *npj Quantum Information* **2**, 16035 (2016), [arXiv:1505.06078 \[physics.atm-clus\]](https://arxiv.org/abs/1505.06078).
- ⁴⁸ M. Ruby, F. Pientka, Y. Peng, F. von Oppen, B. W. Heinrich, and K. J. Franke, *Phys. Rev. Lett.* **115**, 197204 (2015).
- ⁴⁹ M.-X. Wang, C. Liu, J.-P. Xu, F. Yang, L. Miao, M.-Y. Yao, C. L. Gao, C. Shen, X. Ma, X. Chen, Z.-A. Xu, Y. Liu, S.-C. Zhang, D. Qian, J.-F. Jia, and Q.-K. Xue, *Science* **336**, 52 (2012), <http://science.sciencemag.org/content/336/6077/52.full.pdf>.
- ⁵⁰ Q. L. He, L. Pan, A. L. Stern, E. C. Burks, X. Che, G. Yin, J. Wang, B. Lian, Q. Zhou, E. S. Choi, K. Murata, X. Kou, Z. Chen, T. Nie, Q. Shao, Y. Fan, S.-C. Zhang, K. Liu, J. Xia, and K. L. Wang, *SCIENCE* **357**, 294 (2017).
- ⁵¹ D. Wang, L. Kong, P. Fan, H. Chen, S. Zhu, W. Liu, L. Cao, Y. Sun, S. Du, J. Schneeloch, R. Zhong, G. Gu, L. Fu, H. Ding, and H.-J. Gao, *Science* **362**, 333 (2018), <http://science.sciencemag.org/content/362/6412/333.full.pdf>.
- ⁵² H. Ren, F. Pientka, S. Hart, A. T. Pierce, M. Kosowsky, L. Lunczer, R. Schlereth, B. Scharf, E. M. Hankiewicz, L. W. Molenkamp, et al., *Nature* **569**, 93 (2019).
- ⁵³ S. Hart, H. Ren, M. Kosowsky, G. Ben-Shach, P. Leubner, C. Brüne, H. Buhmann, L. W. Molenkamp, B. I. Halperin, and A. Yacoby, *Nature Physics* **13**, 87 (2017).
- ⁵⁴ F. Wilczek, *Nature Physics* **5**, 614 (2009).
- ⁵⁵ A. Stern, *Nature* **464**, 187 (2010).
- ⁵⁶ M. Franz, *Physics* **3**, 24 (2010).
- ⁵⁷ C. Nayak, *Nature* **464**, 693 (2010).
- ⁵⁸ C.-X. Liu, J. D. Sau, T. D. Stanescu, and S. Das Sarma, *Phys. Rev. B* **96**, 075161 (2017).
- ⁵⁹ D. Bagrets and A. Altland, *Phys. Rev. Lett.* **109**, 227005 (2012).
- ⁶⁰ J. Liu, A. C. Potter, K. T. Law, and P. A. Lee, *Phys. Rev. Lett.* **109**, 267002 (2012).
- ⁶¹ D. Pikulin, J. Dahlhaus, M. Wimmer, H. Schomerus, and C. Beenakker, *New Journal of Physics* **14**, 125011 (2012).
- ⁶² E. J. H. Lee, X. Jiang, R. Aguado, G. Katsaros, C. M. Lieber, and S. De Franceschi, *Phys. Rev. Lett.* **109**, 186802 (2012).
- ⁶³ L. Villegas-Lelovsky, C. Trallero-Giner, M. Rebello Sousa Dias, V. Lopez-Richard, and G. E. Marques, *Phys. Rev. B* **79**, 155306 (2009).
- ⁶⁴ J. Soo Lim, R. Lopez, and L. Serra, *EPL (Europhysics Letters)* **103**, 37004 (2013).
- ⁶⁵ C. Lei, H. Chen, and A. H. MacDonald, *Phys. Rev. Lett.* **121**, 227701 (2018).